



Earth's magnetosheath: A comparison of plasma flow direction between models and observations

Marek Vandas¹ and Evgeny Romashets²

Correspondence: Evgeny Romashets (eromashets@lamar.edu)

Abstract. Observations of the plasma flow direction in the Earth's magnetosheath are compared with the help of three analytical magnetic-field models, namely Kobel and Flückiger (1994), Romashets and Vandas (2019), and Vandas and Romashets (2019), which all assume current-free fields in the magnetosheath. 47 magnetosheath passages by spacecraft are analyzed in detail and performance of the models are evaluated. It is concluded that the performances are comparable and that they are satisfactory on average. Therefore, a usage of the model by Kobel and Flückiger (1994) is recommended, because it is the simplest one and yields results much faster.

1 Introduction

Earth's magnetic field represents an obstacle for a flowing solar wind. Because the flow is mostly supersonic, a bow shock (BS) is formed ahead. Earth's magnetic field forms a magnetosphere, which is separated from the interplanetary magnetic field by a thin layer, the magnetopause (MP). The region between the BS and MP is called the magnetosheath (MSH) and contains compressed, heated, and diverted solar-wind plasma with an interplanetary magnetic field draped around the MP.

Modeling of the near-Earth environment started soon after the discovery of the solar wind. First, numerical gasdynamical calculations were performed (Spreiter et al., 1966), followed by MHD simulations intending to include a magnetic field self-consistently (e.g., Spreiter and Stahara, 1980; Siscoe et al., 2002; Samsonov, 2006). Alternatively, there are analytical or semi-empirical models of the MSH magnetic field and plasma flow (Kobel and Flückiger, 1994; Génot et al., 2009; Kallio and Koskinen, 2000; Romashets et al., 2010; Génot et al., 2011; Soucek and Escoubet, 2012; Romashets and Vandas, 2019; Vandas and Romashets, 2019; Tsyganenko et al., 2023, etc.). Models of the MSH are important for knowledge of the conditions near the MP, which by a large part determine changes in geomagnetic activity (e.g., Trattner et al., 2015; Michotte de Welle et al., 2024). The MSH serves as a laboratory for studies of plasma waves, instabilities, and turbulence, which to some extent rely on MSH models (e.g., Tátrallyay and Erdős, 2002).

The aim of this paper is to test selected analytical MSH models against observations. Some tests in a statistical sense over larger MSH regions have been performed (e.g., Kaymaz, 1998; Soucek and Escoubet, 2012; Michotte de Welle et al., 2022). Our approach is similar to that of Turc et al. (2014), who compared observations in the MSH during passages of magnetic

¹Astronomical Institute of the Czech Academy of Sciences, Prague, Czech Republic

²Department of Physics, Lamar University Beaumont, Texas, USA

https://doi.org/10.5194/egusphere-2025-4672 Preprint. Discussion started: 21 October 2025 © Author(s) 2025. CC BY 4.0 License.





clouds with a model. We do a detailed comparison of MSH passages by spacecraft between their measurements and outputs of several models.

Based on our experience gained in Vandas and Romashets (2024), we use here three MSH models which describe potential (current-free) magnetic fields between two confocal paraboloids (Kobel and Flückiger, 1994), two non-confocal paraboloids (Romashets and Vandas, 2019), and two non-confocal spheroids (Vandas and Romashets, 2019). In the cited work, we expected that the model with non-confocal paraboloids would perform better than that with confocal ones, because the geometry of the Vandas and Romashets (2019) model better reflects the reality, but this was not the case. It performed comparatively well.

Kobel and Flückiger (1994) noted that their magnetic field lines in the MSH might serve as flow lines when the upstream magnetic field is radial. Tátrallyay and Erdős (2002), Tátrallyay et al. (2008), and Génot et al. (2009) used this hypothesis when analyzing waves and plasma instabilities in the MSH. Génot et al. (2011) elaborated a comprehensive model of the plasma flow in the MSH, based on this hypotheses and the Kobel and Flückiger (1994) model. Soucek and Escoubet (2012) tested the mentioned flow model with observations in a statistical way and reported a fairly good agreement. Schmid et al. (2021) applied the flow model to the MSH of Mercury, anticipating a future comparison with observations. With the three magnetic-field models in hands here, we test the hypothesis in a way similar to our dealing with magnetic-field observations.

2 Modeling of the plasma flow direction in the MSH

This modeling is based on the hypothesis by Kobel and Flückiger (1994) and Soucek and Escoubet (2012), that flow stream-lines in the MSH would coincide with magnetic field lines when the upstream magnetic field was radial. We procede in this way. Shapes of the BS and MP follow from their models, solar wind dynamic pressure, and real BS and MP crossings, and determine the shape of the MSH for each instance. A model of the MSH magnetic field under the assuption that the upstream magnetic field is radial yields a magnetic field configuration in the MSH, magnetic field lines of which are in fact flow stream-lines (according to the hypothesis). The flow streamlines determine flow directions which can be compared with observed directions, thus testing the hypothesis. We do not model velocity magnitude, because it needs additional assumptions going beyond the scope of this paper.

In the following subsections we describe BS and MP models and MSH magnetic field models used in the present paper. Only analytical models are included. We consider four BS and MP models, and three MSH magnetic-field models, which are potential (current-free) models, two of them assume axially symmetric paraboloidal BS and MP shapes, and the third one is of spheroidal shapes of the BS and MP. Magnetic fields in the MSH depends on BS and MP shapes (i.e., a_{ij} coefficients described below) and on the upstream magnetic field, which is assumed homogeneous. All of these quantities change in time according to varying upstream conditions, that is, the dynamical pressure (specifying the a_{ij} coefficients) and the upstream magnetic field vector, which are known from observations.





55 2.1 BS and MP Shapes

Determination of the BS and MP shapes follows the way described in Vandas and Romashets (2024). We work in abberated coordinate system. Its relationship to the GSE (Geocentric Solar Ecliptic) system is shown in detail in Vandas et al. (2020). Its center is the Earth's center and the x axis is a common rotational symmetry axis for BS and MP models used here. We assume that the BS and MP have spheroidal or paraboloidal shapes (always the same types for both), which are defined by coefficients a_{11} , a_{14} , a_{44} , and equations

$$a_{11,BS}x_{BS}^2 + y_{BS}^2 + z_{BS}^2 + a_{14,BS}x_{BS} + a_{44,BS} = 0,$$
 (1)

$$a_{11,\text{MP}}x_{\text{MP}}^2 + y_{\text{MP}}^2 + z_{\text{MP}}^2 + a_{14,\text{MP}}x_{\text{MP}} + a_{44,\text{MP}} = 0.$$
 (2)

The subscripts BS or MP at coordinates stress that the points are located at the BS or MP. For the time when a satellite crossed the BS, it holds

$$a_{11,\mathrm{BS}}^{(\mathrm{BS})}[x_{\mathrm{BS}}^{(\mathrm{BS})}]^2 + [y_{\mathrm{BS}}^{(\mathrm{BS})}]^2 + [z_{\mathrm{BS}}^{(\mathrm{BS})}]^2 + a_{14,\mathrm{BS}}^{(\mathrm{BS})}x_{\mathrm{BS}}^{(\mathrm{BS})} + a_{44,\mathrm{BS}}^{(\mathrm{BS})} = 0, \tag{3}$$

where $x_{\rm BS}^{\rm (BS)}$, $y_{\rm BS}^{\rm (BS)}$, and $x_{\rm BS}^{\rm (BS)}$ are coordinates of the BS crossing, the time of the BS crossing is indicated by BS in parentheses. Similarly, for the MP crossing, we have

$$a_{11,\text{MP}}^{(\text{MP})}[x_{\text{MP}}^{(\text{MP})}]^2 + [y_{\text{MP}}^{(\text{MP})}]^2 + [z_{\text{MP}}^{(\text{MP})}]^2 + a_{14,\text{MP}}^{(\text{MP})}x_{\text{MP}}^{(\text{MP})} + a_{44,\text{MP}}^{(\text{MP})} = 0.$$
(4)

The coordinates of the crossings are known and we need to determine six a-coefficients. Two equations for them have been just listed, the remaining four are specific for BS and MP models used and will be described later. The coefficients for the BS crossing fix the BS shape for the upstream dynamical pressure $P_{\rm d}^{\rm (BS)}$ (following from data) at this time, and similarly for the MP crossing and corresponding upstream dynamical pressure $P_{\rm d}^{\rm (MP)}$. For a general time and corresponding upstream dynamical pressure, $P_{\rm d}$, the shapes of the BS and MP are given by Eqs. (1)–(2) with

$$a_{11,BS} = a_{11,BS}^{(BS)}, \ a_{14,BS} = a_{14,BS}^{(BS)} \left[\frac{P_{d}^{(BS)}}{P_{d}} \right]^{\frac{1}{\varepsilon_{BS}}}, \ a_{44,BS} = a_{44,BS}^{(BS)} \left[\frac{P_{d}^{(BS)}}{P_{d}} \right]^{\frac{2}{\varepsilon_{BS}}},$$
 (5)

$$a_{11,\text{MP}} = a_{11,\text{MP}}^{(\text{MP})}, \ a_{14,\text{MP}} = a_{14,\text{MP}}^{(\text{MP})} \left[\frac{P_{\text{d}}^{(\text{MP})}}{P_{\text{d}}} \right]^{\frac{1}{\varepsilon_{\text{MP}}}}, \ a_{44,\text{MP}} = a_{44,\text{MP}}^{(\text{MP})} \left[\frac{P_{\text{d}}^{(\text{MP})}}{P_{\text{d}}} \right]^{\frac{2}{\varepsilon_{\text{MP}}}}.$$
 (6)

The last relationships follow from a common assumption in which the BS and MP radially shrink or expand in a dependence on $P_{\rm d}$, more specifically coordinates of BS and MP points behave as $x_{\rm BS} \propto P_{\rm d}^{-\frac{1}{\varepsilon_{\rm BS}}}$, and so on for the other coordinates (note that there are misprints in Eqs. (3) and (6) in Vandas and Romashets (2024), there are missing minus signs in all exponents). The constants $\varepsilon_{\rm BS}$ and $\varepsilon_{\rm MP}$ are specified by the BS and MP models. The dynamical pressure is calculated by the formula $P_{\rm d}=1.2n_{\rm p}m_{\rm p}V_{\rm sw}^2$, where $n_{\rm p}$ is the upstream proton number density, $m_{\rm p}$ is the proton mass, $V_{\rm sw}$ is the upstream solar wind velocity, and the factor 1.2 accounts for the presence of alpha particles (helium) in the solar wind.





2.2 Magnetic Field Model 1

Model 1 is the Kobel and Flückiger (1994) model, which have paraboloidal BS and MP with the same foci, which are situated halfway between the MP nose and the Earth's center (the origin of coordinates). This means that

$$a_{11,BS} = 0, \ a_{11,MP} = 0,$$
 (7)

and the common foci and their placement yield additional two equations

$$\frac{a_{44,BS}}{a_{14,BS}} + \frac{a_{14,BS}}{4} = \frac{a_{44,MP}}{2a_{14,MP}},\tag{8}$$

$$\frac{a_{44,\text{MP}}}{a_{14,\text{MP}}} + \frac{a_{14,\text{MP}}}{4} = \frac{a_{44,\text{MP}}}{2a_{14,\text{MP}}}.$$
(9)

The magnetic field components are given in Kobel and Flückiger (1994). We set $\varepsilon_{\rm BS} = \varepsilon_{\rm MP} = 6$, as commonly used values for them.

85 2.3 Magnetic Field Model 2

Model 2 is the Romashets and Vandas (2019) model, which also have paraboloidal BS and MP but their foci need not coincide. The BS and MP positions and shapes are determined by the Jelínek et al. (2012) model, so we have

$$a_{11,BS} = 0, \ a_{11,MP} = 0,$$
 (10)

$$\frac{a_{44,\text{BS}}}{a_{14,\text{BS}}^2} = -\frac{\lambda_{\text{BS}}^2}{4}, \quad \frac{a_{44,\text{MP}}}{a_{14,\text{MP}}^2} = -\frac{\lambda_{\text{MP}}^2}{4}, \tag{11}$$

with $\lambda_{\rm BS}=1.17$ and $\lambda_{\rm MP}=1.54$. Moreover, $\varepsilon_{\rm BS}=6.55$ and $\varepsilon_{\rm MP}=5.26$. These four values are given in the Jelínek et al. (2012) model. The magnetic field components follow from Romashets and Vandas (2019).

2.4 Magnetic Field Model 3

Model 3 is the Vandas and Romashets (2019) model, which has spheroidal BS and MP, and their foci may not coincide. The BS and MP positions and shapes are determined by simplified Formisano (1979) and Formisano et al. (1979) models, namely that the a_{ij} coefficients save the proportions as in Formisano's BS and MP models,

$$a_{11,BS} = a_{11na,BS}, \frac{a_{14,BS}^2}{a_{44,BS}} = \frac{a_{14na,BS}^2}{a_{44na,BS}}, a_{11,MP} = a_{11na,MP}, \frac{a_{14,MP}^2}{a_{44,MP}} = \frac{a_{14na,MP}^2}{a_{44na,MP}},$$
 (12)

where coefficients with the subscript na are the scaled Formisano's coefficients in the abberated system: $a_{11\text{na,BS}} = 0.52$, $a_{14\text{na,BS}} = 47.53$, $a_{44\text{na,BS}} = -613$, $a_{11\text{na,MP}} = 0.65$, $a_{14\text{na,MP}} = 21.41$, and $a_{44\text{na,MP}} = -221$ (see Vandas et al., 2020). It is set $\varepsilon_{\text{BS}} = \varepsilon_{\text{MP}} = 6$. The magnetic field components are given in Vandas and Romashets (2019).

https://doi.org/10.5194/egusphere-2025-4672 Preprint. Discussion started: 21 October 2025 © Author(s) 2025. CC BY 4.0 License.





3 Data

100

105

We used observations during MSH passages by Cluster, Themis, and MMS spacecraft. There are many such passages but our quite stringent criteria limited cases very much. We required a passage to be at least a few hours long, contained both plasma and magnetic field measurements, BS and MP crossings to be clearly identifiable, and upstream data for moments of BS and MP crossings are known. OMNI data for determination of upstream conditions were utilized. We obtained 47 cases which are listed in Table 1. Columns from left to the right show the case number, spacecraft, time interval of the passage (when the second time is lower than the first time, it means the next day), direction of the passage, and coordinates (in GSE system; units are R_E , where R_E is the Earth's radius) of the satellites at moments of the BS and MP crossings. Note that the coordinates are in capital letters in order to distinguish them from the lower-case coordinates (used, e.g., in Eq. (3)), which are coordinates in the abberated system. Nevertheless, the latter ones are calculated from the former ones using the relationships given in Vandas et al. (2020). Data for the MSH passages were taken from the World Data Center (WDC) at NASA GSFC (http://cdaweb.gsfc.nasa.gov/cdaweb/). We used 1-min averages provided by WDC from Cluster (magnetic field: FGM instrument, PIs A. Balogh & E. Lucek, data source CP FGM SPIN; plasma velocity: CIS instrument, PI H. Rème, data source PP_CIS), Themis (magnetic field: FGM instrument, PIs V. Angelopoulos, U. Auster, K. H. Glassmeier, & W. Baumjohann, data source 12_fgm; plasma velocity: ESA instrument, PIs V. Angelopoulos, C. W. Carlson & J. McFadden, data source 12 mom), and MMS (magnetic field: FGM instrument, PIs J. Burch, C. Russell, & W. Magnus, data source fgm srvy 12; plasma velocity: DIS instrument, PIs J. Burch, C. Pollock, & B. Giles, data source fpi_fast_12_dis-moms). For determination of upstream magnetic field and dynamical pressure, 1-min averages of OMNI Plus data (Wind KP shifted to the BS nose; when not available, ACE_bsn) from WDC (https://omniweb.gsfc.nasa.gov/) were used.

4 Results

We calculated MSH model magnetic field configurations for the MSH passages listed in Table 1 two times, for the upstream magnetic field vector from OMNI, and for the upstream radial field (i.e., only the x component present). Each observation in the MSH (with 1 min cadence) was supplemented by these model magnetic field vectors (calculated at real spacecraft positions and provided that the necessary upstream values were known), and resulting observed and model profiles were compared. It means that for each time, magnetic field configurations were calculated anew, because the upstream plasma dynamic pressure and magnetic field vector generally changed, and so did the positions and shapes of the BS and MP. The modeled magnetic field vectors were uniquely determined by the upstream values and a MSH model used, there were no free parameters or tailoring. Model values with the upstream radial field were used for the determination of the direction of the plasma flow.

An example of the profile comparisons is shown in Figure 1. It is case 7 from Table 1. There are four groups of panels (2×2) , left panels deal with velocity profiles, right panels with magnetic-field profiles in the MSH. Because the velocity magnitude was not modeled, we took it from the observed values for calculations of the modeled velocity vectors, but their directions





Table 1. List of the MSH Crossings.

Case	Spacecraft	Time interval (UT)	Direction	BS crossing			MP crossing		
				$X_{ m BS}^{ m (BS)}$	$Y_{ m BS}^{ m (BS)}$	$Z_{ m BS}^{ m (BS)}$	$X_{\mathrm{MP}}^{\mathrm{(MP)}}$	$Y_{\mathrm{MP}}^{\mathrm{(MP)}}$	$Z_{\mathrm{MP}}^{\mathrm{(MP)}}$
1	Cluster 4	22/01/2002 2:02-10:54	$BS{\to}MP$	13.1	7.4	-6.6	6.3	0.9	-8.4
2	Cluster 4	19/02/2002 17:14-23:42	$BS{\rightarrow}MP$	13.2	-0.6	-7.7	6.0	-2.3	-8.5
3	Cluster 3	7/12/2002 0:19-8:08	$BS{\rightarrow}MP$	4.0	12.0	-9.2	3.5	3.0	-8.8
4	Cluster 4	4/02/2003 13:54-19:25	$BS{\to}MP$	10.8	1.4	-9.2	4.6	-1.6	-8.4
5	Cluster 4	5/02/2003 11:17-16:00	$MP{\rightarrow}BS$	12.5	8.7	5.0	8.3	7.4	6.8
6	Cluster 1	5/01/2004 22:50-5:09	$BS{\to}MP$	9.3	7.9	-10.1	5.8	2.1	-9.8
7	Cluster 4	30/01/2004 16:55-21:32	$MP{\rightarrow}BS$	11.2	9.5	4.1	6.9	7.7	6.1
8	Cluster 4	1/03/2004 12:39-15:52	$MP{\rightarrow}BS$	11.0	2.9	5.6	6.7	3.1	6.5
9	Cluster 4	7/03/2004 21:34-1:58	$BS{\to}MP$	8.9	-4.8	-10.5	3.8	-4.2	-9.7
10	Cluster 4	2/04/2004 21:15-4:07	$BS{\to}MP$	9.3	-9.9	-10.1	3.4	-6.7	-10.3
11	Cluster 3	3/04/2004 18:29-20:42	$MP{\rightarrow}BS$	8.5	-2.0	6.2	5.5	-0.2	6.4
12	Cluster 3	6/03/2005 5:35-10:00	$BS{\to}MP$	8.0	-4.5	-11.5	2.8	-4.1	-9.4
13	Cluster 4	6/02/2006 8:10-12:16	$MP{\rightarrow}BS$	10.8	8.2	2.7	6.5	6.8	5.0
14	Cluster 4	18/02/2006 6:55-10:59	$MP{\rightarrow}BS$	13.3	5.7	1.8	9.3	5.6	4.3
15	Cluster 4	8/05/2006 20:20-4:51	$BS{\rightarrow} MP$	3.8	-15.6	-10.4	0.1	-11.1	-12.0
16	Cluster 4	23/05/2006 1:58-11:11	$BS{\rightarrow} MP$	0.4	-16.6	-10.1	-2.4	-11.1	-12.0
17	Cluster 4	18/01/21.5 21:37-1:05	$BS{\to}MP$	8.6	1.6	-11.4	5.8	-1.0	-9.8
18	Cluster 4	2/02/21.5 0:42-7:44	$BS{\to}MP$	11.4	1.2	-12.0	5.4	-2.4	-9.8
19	Cluster 4	7/03/21.5 10:58–15:47	$BS{\to}MP$	7.9	-5.5	-11.6	2.8	-5.0	-9.5
20	Cluster 4	10/03/21.5 14:35–18:08	$MP{\rightarrow}BS$	13.9	1.3	0.5	10.3	2.3	2.6
21	Cluster 3	24/03/21.5 1:16-5:43	$BS{ ightarrow}MP$	7.3	-7.9	-11.9	3.2	-6.5	-10.5
22	Cluster 3	24/03/21.5 20:23-23:40	$MP{\rightarrow}BS$	13.1	-1.7	0.9	9.7	0.1	2.9
23	Cluster 3	29/03/21.5 15:47–19:03	$MP \rightarrow BS$	13.8	-3.4	0.2	11.0	-1.5	2.2
24	Cluster 3	17/04/21.5 15:44–19:09	$MP \rightarrow BS$	11.6	-7.2	0.5	9.3	-4.2	2.5
25	Cluster 3	19/04/21.5 3:45-10:08	$BS \rightarrow MP$	4.4	-11.2	-12.1	0.0	-7.1	-10.4
26	Themis E	14/07/21.5 5:36–7:12	$MP \rightarrow BS$	12.5	0.1	-3.5	11.5	-1.5	-3.1
27	Themis C	30/09/2008 19:28-21:53	$BS{ ightarrow}MP$	11.8	-3.4	-0.8	9.4	-1.4	0.0
28	Cluster 3	26/01/2009 5:59-7:39	$MP \rightarrow BS$	7.4	11.4	-2.0	5.9	10.4	-1.0
29	Cluster 4	10/05/2009 20:23-0:10	$MP \rightarrow BS$	9.8	-12.1	-4.5	9.1	-9.0	-2.3
30	Cluster 4	7/01/2010 19:44–23:33	$BS \rightarrow MP$	10.2	8.5	-9.7	9.1	5.4	-8.2
31	Cluster 4	19/01/2010 3:33-10:30	$BS \rightarrow MP$	11.6	6.0	-9.6	7.2	0.5	-5.7
32	Cluster 4	27/01/2011 8:23–12:22	$BS \rightarrow MP$	12.2	3.9	-8.1	9.7	1.2	-5.6
33	Cluster 4	23/02/2011 8:45–14:02	$BS \rightarrow MP$	14.4	-1.3	-9.4	10.9	-3.1	-6.5
34	Cluster 4	15/12/2012 17:25–8:55	$MP \rightarrow BS$	4.1	16.8	-11.0	-1.6	11.0	-12.0
35	Cluster 4	16/12/2012 17:55–2:55	$BS \rightarrow MP$	6.5	15.8	-7.4	7.1	10.6	-1.8
36	MMS 1	7/10/2015 13:46–18:45	$BS \rightarrow MP$	7.2	9.5	-0.6	3.7	9.2	-0.8
37	MMS 1	25/12/2015 5:40–10:42	$BS \rightarrow MP$	11.3	-3.6	-1.1	9.4	-0.3	-0.9
38	MMS 2	8/11/21.5 1:29–8:25	$BS \rightarrow MP$	4.0	19.2	6.0	0.8	14.7	4.8
39	MMS 1	19/11/21.5 12:12–16:22	$BS \rightarrow MP$	5.2	15.9	5.4	2.5	12.9	4.4
40	MMS 1	9/02/2018 22:24–1:00	$MP \rightarrow BS$	8.8	-10.5	3.1	6.0	-9.0	2.2
41	MMS 1	14/02/2018 23:49–2:40	BS→MP	14.0	-2.1	4.5	11.1	-0.4	3.5
42	MMS 1	24/02/2018 0:25-4:42	MP→BS	7.4	-13.2	3.8	3.6	-10.0	2.3
43	MMS 1	21/11/2018 8:45–17:16	MP→BS	11.0	13.4	6.5	7.9	5.0	3.7
44	MMS 1	16/01/2019 4:18–6:48	BS→MP	11.1	8.0	2.1	8.1	7.2	1.2
45	MMS 1	18/01/2019 22:21-0:29	BS→MP	13.2	7.7	2.6	10.9	7.3	1.9
46	MMS 1	12/02/2019 0:13–2:11	BS→MP	13.1	2.8	1.4	10.4	3.2	1.5
47	MMS 1	13/04/2019 8:10-13:16	MP→BS	1.3	-20.2	7.7	-0.5	-16.5	6.9



140

150



Table 2. Performance of the Models According to δ_{avg}

Model	Best model (%)	Average rank	Average $\delta_{\rm avg}$
1	19	2.02	4.51°
2	28	2.13	4.50°
3	53	1.85	4.51°

followed from the modeled values. The δ is the angle between the observed and modeled velocity vectors,

$$\delta = \arccos \frac{V^{\text{(obs)}} \cdot B^{\text{(rmod)}}}{|V^{\text{(obs)}}| |B^{\text{(rmod)}}|}$$
(13)

where $B^{(\mathrm{rmod})}$ is a modeled magnetic field in the MSH when the upstream magnetic field is radial. A low value of δ indicates a good match in the flow direction. Top groups of panels in Figure 1 show results for Model 1, bottom groups for Model 2 for comparison. We see that the modeled profiles follow relatively well the observed ones in this case for both the magnetic field and velocity. Larger discrepancies are mainly near the MP, a feature already noticed in our previous papers. In addition, we can see that there are no significant differences in the results between Models 1 and 2. Therefore in the following figures with profiles we display only that for Model 1. One can observe that quite large variations in the magnetic field components are relatively well matched by the model.

Figure 2 displays case 43 when a large change in the dynamical pressure occurred. The observed profiles are quite well matched by modeled ones. If magnetic field profiles are satisfactorily met by a model, it does not guarantee that velocity directions will be met, as Figure 3 demonstrates, and vice versa (Figure 4). Figure 5 is an example when models fail for both magnetic field and velocity directions.

The quality of the plasma-flow-direction match was measured by averaged δ 's (Eq. (13)) for each case,

$$\delta_{\text{avg}} = \frac{1}{N} \sum_{i=1}^{N} \delta_i = \frac{1}{N} \sum_{i=1}^{N} \arccos \frac{\boldsymbol{V}_i^{(\text{obs})} \cdot \boldsymbol{B}_i^{(\text{rmod})}}{|\boldsymbol{V}_i^{(\text{obs})}| |\boldsymbol{B}_i^{(\text{rmod})}|}$$
(14)

where N is a number of compared values for a given passage. We used this measure to summarize results over all our cases. For each case, we ranked the three models according to values δ_{avg} as 1 (the best, i.e., it has a lowest value), 2, or 3.

Table 2 lists percentages when the models were the best (the second column) and averaged ranks over cases (the third column). We see that differences among models are marginal. The δ_{avg} averaged over cases is practically the same for all models, and it is satisfactorily low, indicating on average an acceptable agreement between magnetic field lines of a particular magnetic field configuration and flow lines.

Figure 6a shows a dependency of our quality measure $\delta_{\rm avg}$ on $D_{\rm st}$. A $D_{\rm st}$ value for a particular case means its average over the related MSH passage. And it is also done in such a way for the other quantities shown in the other panels. One can see that there are no significant differences in behavior of the models, but there are large fluctuations in values and no neat dependency. We can only judge on trends making linear regression in a form of dashed lines with the same color coding as for the solid lines. The models of the MSH plasma flow perform slightly worse with increasing geomagnetic activity. A similar situation is with





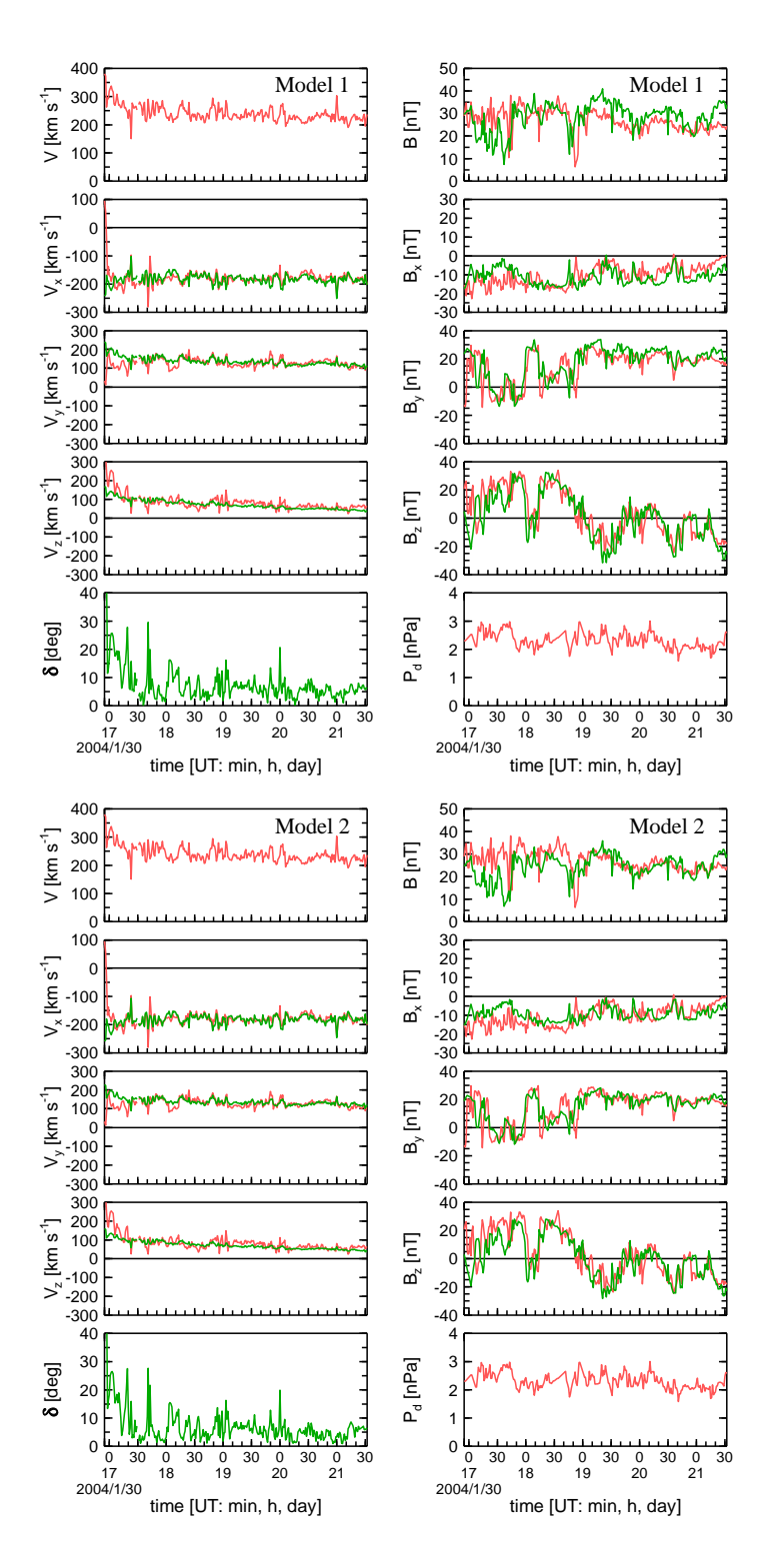


Figure 1. Observed (red lines) and modeled (green lines) quantities for the passage through the Earth's MSH in case 7. Left panels: from top the velocity magnitude V, GSE velocity components V_x , V_y , and V_z , and the angle δ between the observed and modeled velocity vectors; right panels: from top the magnetic field magnitude B, GSE magnetic field components B_x , B_y , and B_z , and upstream dynamic pressure $P_{\rm d}$. Upper panels are for Model 1, bottom panels for Model 2.





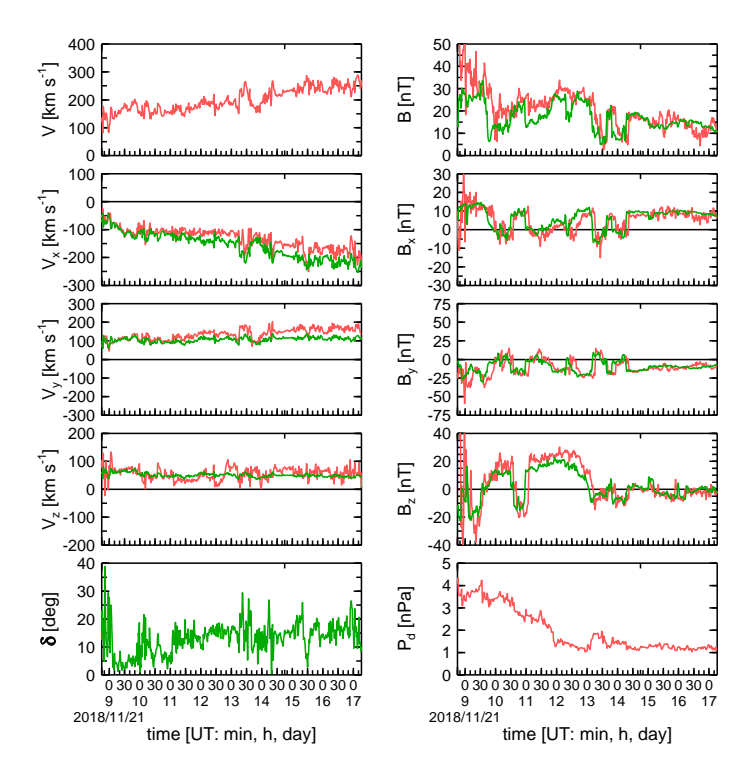


Figure 2. Observed and modeled quantities in the MSH for case 43. Only results of Model 1 are shown, otherwise the format is the same as for Figure 1.

the dynamical pressure $P_{\rm d}$ (Figure 6b). Agreement with the model plasma flow directions becomes worse with a $P_{\rm d}$ increase. There is no trend for the upstream solar wind velocity $V_{\rm sw}$ (Figure 6c), so there must be an increase in $\delta_{\rm avg}$ with increasing upstream density $n_{\rm p}$, as Figure 6d confirms. The trend for the upstream magnetic-field cone angle θ_B (Figure 6e) indicates that the plasma flow directions are better modeled when the upstream magnetic field is close to radial. Figure 6f) shows that the flow direction is modeled worser for low cone angles $\theta_{\rm CBS}$ of the BS crossing point (closer to the subsolar point).

5 Conclusions

155

We examined plasma flow directions in the MSH and compared them with modeled quantities. Three current-free MSH models were used and the hypothesis that flow lines coincide with magnetic field lines when the upstream magnetic field is set radial. The quality of the match was measured by the averaged angle between the observed and modeled plasma flow directions. We found that there are no significant differences in the performances of the models. The models yielded directions of the plasma flow quite satisfactorily on average, the difference averaged over all cases was about 4.5° only. Contrary to the magnetic field modeling, in the case of plasma-flow modeling, the performances mildly depend on values of the dynamic pressure or





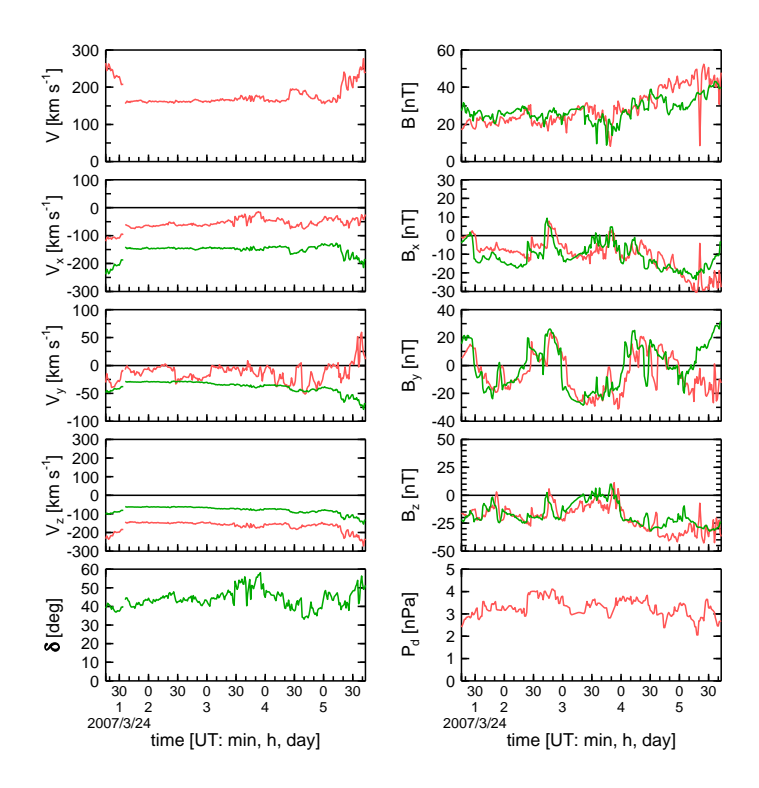


Figure 3. Observed and modeled quantities in the MSH for case 21. The format is the same as in Figure 2.

165 geomagnetic activity (worse with higher values). The models better describes the plasma flow directions for passages farther from the subsolar point, or when the upstream magnetic field is closer to radial.

Because the performances of the models are comparable, we recommend to use the Kobel and Flückiger (1994) model, which is simpler and much more faster in yielding results than the other models.

Data availability. The data were provided by the World Data Center at NASA GSFC.

170 Author contributions. M.V. suggested the method and performed calculations, both authors analyzed data, wrote the text and made editing.

Competing interests. No competing interests are present.





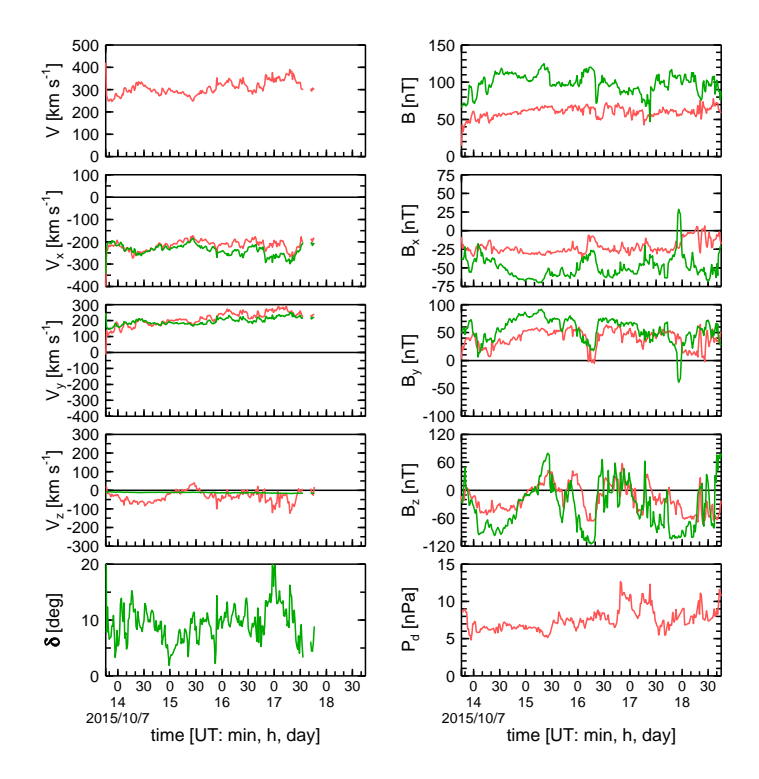


Figure 4. Observed and modeled quantities in the MSH for case 36. The format is the same as in Figure 2.

Acknowledgements. This work was supported by the NSF grant 2230363. M. V. acknowledges support from the AV ČR grant RVO:67985815 and the GAČR grant 21-26463S.





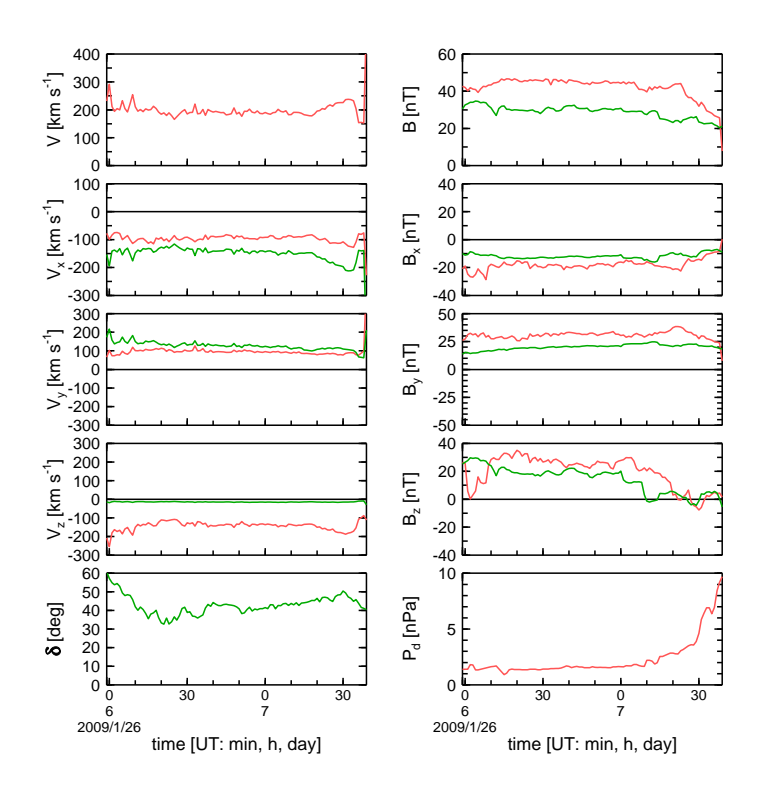


Figure 5. Observed and modeled quantities in the MSH for case 28. The format is the same as in Figure 2.

References

- Formisano, V.: Orientation and shape of the Earth's bow shock in three dimensions, Planet. Space Sci., 27, 1151–1161, 1979.

 Formisano, V., Domingo, V., and Wenzel, K.-P.: The three-dimensional shape of the magnetopause, Planet. Space Sci., 27, 1137–1149, 1979.

 Génot, V., Budnik, E., Hellinger, P., Passot, T., Belmont, G., Trávníček, P. M., Sulem, P.-L., Lucek, E., and Dandouras, I.: Mirror structures above and below the linear instability threshold: Cluster observations, fluid model and hybrid simulations, Ann. Geophys., 27, 601–615, https://doi.org/10.5194/angeo-27-601-2009, 2009.
- Génot, V., Broussillou, L., Budnik, E., Hellinger, P., Trávníček, P. M., Lucek, E., and Dandouras, I.: Timing mirror structures observed by Cluster with a magnetosheath flow model, Ann. Geophys., 29, 1849–1860, https://doi.org/10.5194/angeo-29-1849-2011, 2011.
 - Jelínek, K., Němeček, Z., and Šafránková, J.: A new approach to magnetopause and bow shock modeling based on automated region identification, J. Geophys. Res., 117, A05208, https://doi.org/10.1029/2011JA017252, 2012.
- Kallio, E. J. and Koskinen, H. E. J.: A semiempirical magnetosheath model to analyze the solar wind–magnetosphere interaction, J. Geophys. Res., 105, 27 469–27 480, https://doi.org/10.1029/2000JA900086, 2000.
 - Kaymaz, Z.: IMP 8 magnetosheath field comparisons with models, Ann. Geophys., 16, 376, https://doi.org/10.1007/s00585-998-0376-3, 1998.
 - Kobel, E. and Flückiger, E. O.: A model of the steady state magnetic field in the magnetosheath, J. Geophys. Res., 99, 23 617–23 622, 1994.





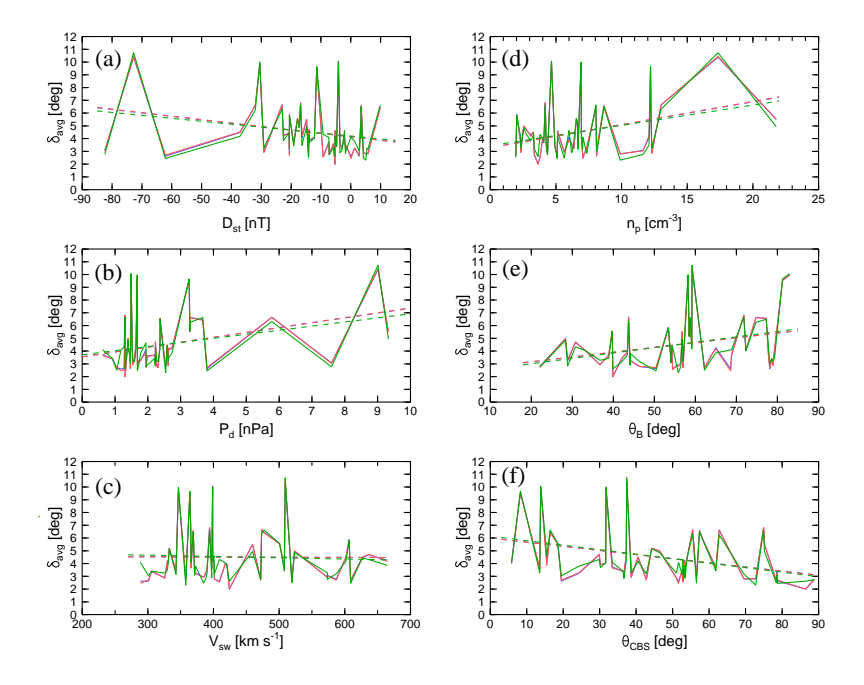


Figure 6. Dependencies of δ_{avg} on various quantities. The details are given in the text. Model 1 is drawn in the blue line, Model 2 in the red line, and Model 3 in the green line.

- Michotte de Welle, B., Aunai, N., Nguyen, G., Lavraud, B., Génot, V., Jeandet, A., and Smets, R.: Global three-dimensional draping of magnetic field lines in Earth's magnetosheath from in-situ spacecraft measurements, J. Geophys. Res., 127, e2022JA030996, https://doi.org/10.1029/2022JA030996, 2022.
 - Michotte de Welle, B., Aunai, N., Lavraud, B., Génot, V., Nguyen, G., Ghisalberti, A., Smets, R., and Jeandet, A.: Global environmental constraints on magnetic reconnection at the magnetopause from in situ measurements, J. Geophys. Res., 129, e2023JA032098, https://doi.org/10.1029/2023JA032098, 2024.
- Romashets, E., Vandas, M., and Veselovsky, I. S.: Analytical description of electric currents in the magnetosheath region, J. Atm. Sol.-Terr. Phys., 72, 1401–1407, 2010.
 - Romashets, E. P. and Vandas, M.: Analytic modeling of magnetic field in the magnetosheath and outer magnetosphere, J. Geophys. Res., 124, 2697–2710, https://doi.org/10.1029/2018JA026006, 2019.
 - Samsonov, A.: Numerical modelling of the Earth's magnetosheath for different IMF orientations, Adv. Space Res., 38, 1652–1656, 2006.
- Schmid, D., Narita, Y., Plaschke, F., Volwerk, M., Nakamura, R., and Baumjohann, W.: Magnetosheath plasma flow model around Mercury, Ann. Geophys., 39, 563–570, https://doi.org/10.5194/angeo-39-563-2021, 2021.
 - Siscoe, G. L., Erickson, G. M., Sonnerup, B. U. Ö., Maynard, N. C., Schoendorf, J. A., Siebert, K. D., Weimer, D. R., White, W. W., and Wilson, G. R.: Hill model of transpolar potential saturation: comparisons with MHD simulations, J. Geophys. Res., 107, 1075, 2002.
- Soucek, J. and Escoubet, C. P.: Predictive model of magnetosheath plasma flow and its validation against Cluster and THEMIS data, Ann.

 Geophys., 30, 973–982, https://doi.org/10.5194/angeo-30-973-2012, 2012.

https://doi.org/10.5194/egusphere-2025-4672 Preprint. Discussion started: 21 October 2025 © Author(s) 2025. CC BY 4.0 License.



215



- Spreiter, J. R. and Stahara, S. S.: A new predictive model for determining solar wind-terrestrial planet interactions, J. Geophys. Res., 85, 6769–6777, https://doi.org/10.1029/JA085iA12p06769, 1980.
- Spreiter, J. R., Summers, A. L., and Alksne, A. Y.: Hydromagnetic flow around the magnetosphere, Planet. Space Sci., 14, 223–253, https://doi.org/10.1016/0032-0633(66)90124-3, 1966.
- Tátrallyay, M. and Erdős, G.: The evolution of mirror mode fluctuations in the terrestrial magnetosheath, Planet. Space Sci., 50, 593–599, https://doi.org/10.1016/S0032-0633(02)00038-7, 2002.
 - Tátrallyay, M., Erdős, G., Balogh, A., and Dandouras, I.: The evolution of mirror type magnetic fluctuations in the magnetosheath based on multipoint observations, Adv. Space Res., 41, 1537–1544, https://doi.org/10.1016/j.asr.2007.03.039, 2008.
 - Trattner, K. J., Onsager, T. G., Petrinec, S. M., and Fuselier, S. A.: Distinguishing between pulsed and continuous reconnection at the dayside magnetopause, J. Geophys. Res., 120, 1684–1696, https://doi.org/10.1002/2014JA020713, 2015.
 - Tsyganenko, N. A., Semenov, V. S., and Erkaev, N. V.: Data-based modeling of the magnetosheath magnetic field, J. Geophys. Res., 128, e2023JA031665, https://doi.org/10.1029/2023JA031665, 2023.
 - Turc, L., Fontaine, D., Savoini, P., and Kilpua, E.: Magnetic clouds' structure in the magnetosheath as observed by Cluster and Geotail: Four case studies, Ann. Geophys., 32, 1247–1261, https://doi.org/10.5194/angeo-32-1247-2014, 2014.
- Vandas, M. and Romashets, E.: Magnetic field in the Earth's magnetosheath: Models versus observations, J. Geophys. Res., 129, e2023JA032393, https://doi.org/10.1029/2023JA032393, 2024.
 - Vandas, M. and Romashets, E. P.: Modeling of magnetic field in the magnetosheath using elliptic coordinates, Planet. Space Sci., 178, 104692, https://doi.org/10.1016/j.pss.2019.07.007, 2019.
- Vandas, M., Němeček, Z., Šafránková, J., Romashets, E. P., and Hajoš, M.: Comparison of observed and modeled magnetic fields in the Earth's magnetosheath, J. Geophys. Res., 125, e27705, https://doi.org/10.1029/2019JA027705, 2020.